Published in final edited form as:

Nature. 2015 February 5; 518(7537): 68–73. doi:10.1038/nature14158.

Transport domain unlocking sets the uptake rate of an aspartate transporter

Nurunisa Akyuz[1], **Elka R. Georgieva**[2,3], **Zhou Zhou**[1], **Sebastian Stolzenberg**[1], **Michel A. Cuendet**[1,4], **George Khelashvili**[1], **Roger B. Altman**[1], **Daniel S. Terry**[1], **Jack H. Freed**[2,3], **Harel Weinstein**[1,5], **Olga Boudker**[1,*], and **Scott C. Blanchard**[1,6,*]

[1] Department of Physiology and Biophysics, Weill Cornell Medical College, 1300 York Avenue, New York, NY 10064, USA [2] National Biomedical Center for Advanced ESR Technology, Cornell University, Ithaca, New York, USA [3] Department of Chemistry and Chemical Biology, Cornell University, Ithaca, New York, USA [4] Swiss Institute of Bioinformatics, Lausanne, Switzerland [5] HRH Prince Alwaleed Bin Talal Bin Abdulaziz Alsaud Institute for Computational Biomedicine, Weill Cornell Medical College, Cornell University, New York, USA [6]Tri-Institutional Training Program in Chemical Biology, New York, NY, USA

Abstract

Glutamate transporters terminate neurotransmission by clearing synaptically released glutamate from the extracellular space, allowing repeated rounds of signaling and preventing glutamate-mediated excitotoxicity. Crystallographic studies on an archaeal homologue, Glt_{Ph}, showed that distinct transport domains translocate substrates into the cytoplasm by moving across the membrane within a central trimerization scaffold. Here, we report direct observations of these 'elevator-like' transport domain motions in the context of reconstituted proteoliposomes and physiological ion gradients using single-molecule fluorescence resonance energy transfer (smFRET) imaging. We show that Glt_{Ph} bearing two “humanizing” mutations exhibits markedly increased transport domain dynamics, which parallels an increased rate of substrate transport, thereby establishing a direct temporal relationship between transport domain motions and substrate uptake. Crystallographic and computational investigations reveal that these mutations favor structurally “unlocked” states with increased solvent occupancy at the interface between the transport domain and the trimeric scaffold.

* Co-corresponding authors Correspondence should be addressed to scb2005@med.cornell.edu and olb2003@med.cornell.edu.

Author contributions: NA, OB and SCB designed the study. NA designed and performed the majority of the experiments and simulated smFRET data. NA analyzed the smFRET data, with support from DT and SCB. NA and OB analyzed crystallographic data. ERG performed and analyzed DEER experiments and ERG and JHF interpreted the data. ZZ synthesized the 4S(COT)-maleimide cyanine dyes. DT made improvements to the smFRET instrumentation and analysis software. RBA prepared reagents for smFRET experiments. HW and MAC designed, and SS, GK, and MAC carried out the MD simulations. NA, OB and SCB, HW and MAC interpreted results and wrote the manuscript.

Author Information: Crystallographic model has been deposited in the Protein Data Bank under accession number 4X2S. Reprints and permissions information is available at www.nature.com/reprints. Authors declare RBA and SCB as co-founders of Lumidyne Corporation.

Glutamate transporters, also termed excitatory amino acid transporters (EAATs), maintain glutamate concentration gradients across the cell membrane by coupling neurotransmitter uptake to symport of three sodium (Na^+) ions and a proton and counter-transport of a potassium ion[1]. Structural information on the EAAT family principally stems from investigations of Glt_{Ph}[2-6], an aspartate and Na^+ symporter[7,8] from *Pyrococcus horikoshii*. Crystal structures of Glt_{Ph} revealed that the homo-trimeric protein is composed of a rigid, central trimerization scaffold that houses three peripheral transport domains containing the substrate binding sites (**Fig. 1a**). Comparison of Glt_{Ph} structures captured in distinct conformations suggests that within the trimerization scaffold, individual transport domains undergo relocations approximately 15 Å normal to the membrane, providing substrate and ions alternating access to the extracellular (outward) and intracellular (inward) solutions (**Extended Data Fig. 1a**)[5].

Single-molecule imaging of Glt_{Ph} provided direct evidence for 'elevator-like' transport domain motions[9,10]. Consonant with double electron-electron spin resonance (DEER) measurements[11,12], these measurements also showed that individual Glt_{Ph} transport domains transition spontaneously between outward- and inward-facing conformations both when free of cargo (apo) and when bound to substrates. Notably, these transport domain motions exhibited heterogeneous dynamic behaviors, alternating between periods of rapid transitions and periods of quiescence[9]. In contrast to observations in structurally unrelated neurotransmitter sodium symporters[13], substrate binding decreased transport domain dynamics in Glt_{Ph} by favoring the quiescent periods such that the frequency of domain motions converged to the substrate uptake rate[7,9].

These findings led to the hypothesis that Glt_{Ph} configurations observed in crystal structures[2,4], showing tight lock-and-key interactions between transport and trimerization domains, represent quiescent "locked" states with high substrate affinity, whereas the short-lived states sampled during dynamic periods are structurally distinct and likely have intrinsically lower substrate affinity (**Extended Data Fig. 1b**). This model posits that transport domain motions require a rate-limiting, structural "unlocking" process that changes the interface between the transport and trimerization domains, likely enabling solvent penetration into that interface[5,9,14].

To assess the relationship between Glt_{Ph} function, dynamics and structure, we employed smFRET imaging in the context of reconstituted proteoliposomes with physiological ion gradients. We compared wild-type (WT) Glt_{Ph} to a gain-of-function, "humanized" (H) mutant R276S/M395R ($H_{276,395}$-Glt_{Ph}), which exhibits a faster rate of substrate uptake[15]. The smFRET experiments revealed that the mutations destabilized quiescent "locked" states. The resulting increase in dynamics paralleled a decreased affinity for substrate and an increased transport rate. Crystallographic analyses supported this observation, showing that the transport domains of $H_{276,395}$-Glt_{Ph} can adopt inward-facing conformations in which the transport domain-trimerization scaffold interface is dramatically more open than previously observed. Computational modeling further suggested that increased solvation by lipid or detergent hydrophobic tails in this interface likely facilitates the formation of such conformations. These observations provide a structural rationale for functional distinctions

between Glt_{Ph} and the human EAATs, and establish a kinetic framework for understanding how regulation can be achieved.

Experimental design

Glt_{Ph} is a structural homologue of EAATs (~35% sequence identity)[2] that preferentially transports aspartate over glutamate, with higher substrate binding affinity and slower uptake rate[3,7]. Ryan and colleagues suggested[15] that these distinctions may stem, in part, from the differential location of a conserved arginine residue[16] that is proximal both to the substrate-binding site and the transport domain-trimerization scaffold interface. While the location of this arginine can differ in the primary sequences of glutamate transporter homologues, its position is conserved in most family members (**Fig. 1a-b, Extended Data Fig. 1c**). In human EAAT1, moving this arginine from trans-membrane segment (TM) 8 to helical hairpin (HP) 1 (where it is located in Glt_{Ph}) markedly increases substrate affinity and decreases uptake rate[15]. Reciprocal mutagenesis of Glt_{Ph}, whereby the arginine is moved from HP1 to TM8 (R276S/M395R), reduces aspartate affinity and increases the transport rate[15]. We took advantage of this gain-of-function mutant to probe correlations between uptake rate and transport domain dynamics.

We performed a comparative analysis of WT and $H_{276,395}$-Glt_{Ph} proteins using smFRET, where elevator-like transport domain motions in individual Glt_{Ph} trimers, bearing one donor and one acceptor fluorophore, were revealed as time-dependent changes in FRET efficiency[9] (**Extended Data Fig. 2a-b**). To investigate such motions in the context of proteoliposomes, we labeled Glt_{Ph} proteins with intra-molecularly stabilized Cy3 and Cy5 derivatives that exhibit intrinsically enhanced brightness and photostability[17,18] (**Extended Data Fig. 2c**), eliminating the need for fluorophore protective agents that disturb lipid bilayer properties[19]. The labeled proteins were reconstituted into liposomes in the absence of substrates for smFRET and bulk substrate uptake measurements. Bulk, radioactive aspartate uptake experiments confirmed that both labeled WT and $H_{276,395}$-Glt_{Ph} mutant transported substrate with rates similar to those of the unlabeled proteins, the mutant being about 4-fold faster than the WT (**Fig. 1c**).

For smFRET measurements, reconstitution procedures were established to yield maximally 1 Glt_{Ph} trimer per vesicle. Proteoliposomes were immobilized *via* biotinylated, fluorescently labeled Glt_{Ph} within passivated quartz microfluidics chambers activated with a biotin-streptavidin bridge (**Fig. 1d**). Using this strategy, only those proteoliposomes containing Glt_{Ph} oriented with the extracellular side facing the vesicle exterior were immobilized and imaged[20]. Imaging experiments were initiated in the absence of substrates under isoelectric conditions and chemical gradients were established by rapidly exchanging the proteoliposomes into a buffer containing Na^+ ions and aspartate. Additionally, we examined the behaviors of the labeled proteins in detergent micelles that afford increased statistics and higher signal-to-noise ratios.

Transport rate and dynamics are correlated

In both the absence and presence of gradients, WT Glt_{Ph} in proteoliposomes showed spontaneous transitions between low-, intermediate- and high-FRET efficiency states

centered at ~0.4, ~0.6 and ~0.9, respectively (**Fig. 1e, f, Extended Data Fig. 3**). In detergent solutions, these FRET states were assigned to specific Glt_{Ph} configurations: the low-FRET state reflects symmetric outward-facing and asymmetrically outward- and inward-facing configurations; intermediate- and high-FRET states reflect, respectively, asymmetrically inward- and outward-facing and simultaneously inward-facing protomers (**Extended Data Fig. 2**)[9]. In line with previous investigations[9,11,12], population FRET data from hundreds of individual proteins in the absence of gradients show that the transporter occupies the outward-facing, low-FRET state about half of the time in both detergent (46%) and lipid vesicles (54%) (Fig. 2a, Extended Data Fig. 3b and Extended Data Table 1a-b). Transitions between low- and higher-FRET states reflect elevator-like movements of the individual transport domains between outward- and inward-facing configurations, respectively[9]. In proteoliposomes, such transitions occurred at a rate of ~0.2 s^{-1}, roughly two-fold less frequently than in detergent (**Extended Data Fig. 3c and Fig. 2a**). Paralleling the effects of substrate binding to WT Glt_{Ph} in detergent (**Fig. 2b**), a modest population shift toward the outward-facing, low-FRET state occurred under active transport conditions achieved by addition of Na^+ and aspartate (**Extended Data Fig. 3b and Extended Data Table 1a-b**). Na^+ and aspartate also reduced transport domain dynamics by 10-fold to ~0.02 s^{-1} (**Extended Data Fig. 3c and Fig. 1f**). Thus, in the presence of chemical gradients the frequency of transitions from outward- to inward-facing state (~0.01 s^{-1}) mirrored the rate of radioactive substrate uptake (~0.007 s^{-1}) (**Fig. 1c**).

Notably, the $H_{276,395}$-Glt_{Ph} mutant only exhibited transitions between low- (0.4) and a single, higher- (0.65) FRET state in both proteoliposomes and detergent (**Fig. 1f, Fig. 2c, Extended Data Fig. 3**). Similarly to the WT protein in the absence of chemical gradients, the low-FRET state was occupied 60% of the time in detergent micelles and 40% in proteoliposomes (**Extended Data Table 1a-b**). The observed FRET transition frequency for $H_{276,395}$-Glt_{Ph} was also two times slower in proteoliposomes (~0.13 s^{-1}) compared to detergent (~0.22 s^{-1}) (**Extended Data Fig. 3c and Fig. 2d**).

In stark contrast to the WT protein, however, the transition frequency in $H_{276,395}$-Glt_{Ph} decreased by less than 2-fold to ~0.1 s^{-1} when transport-supporting chemical gradients were established (**Fig. 1e, f; Extended Data Fig. 3c**). Here again, the frequency of transitions from the outward- to inward-facing FRET state (~0.05 s^{-1}) converged to the measured rate of substrate uptake (~0.03 s^{-1}) (**Fig. 1c**). The quantitative correspondence observed between the rates of smFRET transitions and uptake for the WT and $H_{276,395}$-Glt_{Ph} mutant proteins provides compelling evidence that elevator-like motions of transport domains mediate solute uptake and are critical steps of the transport cycle[9]. This finding was independent of the proteoliposome immobilization strategy used and valinomycin-mediated electrical potentials (**Extended Data Fig. 4a-d**)[10].

$H_{276,395}$-Glt_{Ph} samples a distinct inward-facing state

In contrast to WT Glt_{Ph}, which samples intermediate- (0.6) and high- (0.9) FRET states, $H_{276,395}$-Glt_{Ph} samples only a single higher-FRET (0.65) configuration (**Extended Data Fig. 3**). No excursions into the 0.9 FRET state were observed even when data were collected at 6-fold higher time resolution (15 ms) (**Extended Data Fig. 4e-f**). The absence of the 0.9

FRET state would be expected if only one protomer within the $H_{276,395}$-Glt_{Ph} trimer transitioned into inward-facing configuration at a time, while the formation of symmetric inward-facing states were disallowed. This model is, however, inconsistent with data showing that individual transport domains function independently[5,14,21,22]. An alternative hypothesis is that the inward/outward and inward/inward configurations in $H_{276,395}$-Glt_{Ph} exhibit altered, overlapping FRET values. If this model is correct, then the gain-of-function mutations in $H_{276,395}$-Glt_{Ph} have altered the nature of the elevator-like transport domain motions and the structure of the inward-facing state.

The energy landscape of $H_{276,395}$-Glt_{Ph} is altered

Na^+ and aspartate significantly stabilized the higher-FRET state of $H_{276,395}$-Glt_{Ph} in detergent micelles (**Fig. 2c and Extended Data Table 1a-b**). In detergent, Na^+ and aspartate have access to both the extracellular and cytoplasmic sides of the protein. Assuming that a binding equilibrium is established in each conformation, these observations suggest that substrates bind more tightly to the inward-facing $H_{276,395}$-Glt_{Ph} conformation. Such a response was not observed for the WT Glt_{Ph}, where substrate affinities of the inward- and outward-facing conformations are nearly the same[23] and ligands stabilize the latter only slightly[9,11,12] (**Fig. 2a and Extended Data Table 1**). Notably, the transporter blocker DL-threo-β-benzyloxyaspartate (TBOA)[24] stabilized the outward-facing low-FRET states of both WT and $H_{276,395}$-Glt_{Ph} (**Fig. 2 and Extended Data Fig. 5a-b**). As above, this suggests that TBOA preferentially binds to the outward-facing state of both isoforms. Results consistent with these findings were obtained from ensemble DEER measurements using the protein spin-labeled on the same residue (**Extended Data Fig. 5c**).

Interestingly, the addition of Na^+ and aspartate to $H_{276,395}$-Glt_{Ph} proteoliposomes led to an increase in the outward-facing, low-FRET population (**Extended Data Fig. 3**). This liposome-specific response to substrate addition provides supporting evidence for bilayer integrity. It also reveals that elevator-like transport domain movements –as opposed to substrate release –are rate-limiting in the $H_{276,395}$-Glt_{Ph} transport cycle. If substrate release were slow compared to the domain movements, the state distributions during uptake would mirror those observed in detergent, i.e. show preference for the inward-facing higher-FRET state.

The effect of substrate on the distribution of FRET states observed for both isoforms was concentration-dependent in detergent micelles. Notably, $H_{276,395}$-Glt_{Ph} exhibited an ~1000-fold increase in apparent substrate dissociation constant (K_D) compared to the WT protein (**Fig. 3 and Extended Data Fig. 6a**). This finding was corroborated by bulk measurements (**Extended Data Fig. 6b-c**). Hence, the $H_{276,395}$-Glt_{Ph} mutations affect both transport domain dynamics and substrate affinity even though neither of the mutated residues coordinates aspartate directly in the existing crystal structures. These observations support the hypothesis that substrate binding and transport domain dynamics are physically coupled.

Locked states are destabilized in $H_{276,395}$-Glt_{Ph}

The coexistence of quiescent and dynamic periods evidenced both in the absence and presence of ligands is a hallmark kinetic feature of WT Glt_{Ph}[9]. Binding of Na^+ and aspartate

increases the prevalence of quiescent periods and thus the average FRET state lifetimes (**Fig. 4a,b**). Strikingly, no evidence was found for quiescent periods in the $H_{276,395}$-Glt_{Ph} mutant (**Fig. 4c**) and rapid transport domain dynamics persisted even in the presence of saturating substrate concentrations (**Fig. 2d; Extended Data Table 1c**). These dynamic processes were efficiently blocked by TBOA (**Fig. 2b,d**) consistent with their putative role in substrate transport. In $H_{276,395}$-Glt_{Ph}, substrate binding increased the lifetime of the high-FRET state (~7-fold), with no detectable impact on the low-FRET state lifetime (**Fig. 4d**). In both the absence and presence of ligands, the low- and higher-FRET state lifetimes were monodisperse (**Fig. 4c,d; Extended Data Table 1c**). These findings suggest that in $H_{276,395}$-Glt_{Ph}, the isomerization steps leading to locked configurations of the WT protein are dramatically altered or inaccessible under the conditions examined, although an allosteric coupling between substrate binding and stabilization of the domain interface still exists.

Structure of the inward-facing $H_{276,395}$-Glt_{Ph}

To probe the underpinnings of the altered properties of $H_{276,395}$-Glt_{Ph}, we determined a crystal structure of the protein bound to Na^+ ions and aspartate at a moderate resolution of ~4.5 Å (**Extended Data Fig. 7**). As expected from smFRET experiments (**Fig. 2c**), the structural model clearly showed that all protomers in the trimer spontaneously adopted inward-facing configurations. The model also revealed that the transport domains orientations differed from those previously captured in Glt_{Ph} structures, both with and without stabilizing cross-links[4,5]. Moreover, the trimer was asymmetric, with the transport domain of protomer A assuming a position distinct from the other two.

In protomer A, the transport domain shifted further inward by 2 Å and rotates by 7° around an axis roughly perpendicular to the membrane plane with respect to the WT (**Fig. 5a**). This rearrangement is accommodated by a concerted movement of helices in the scaffold domain, comprising TM1 and peripheral portions of TM2 and TM5 (**Extended Data Fig. 7c**), whose flexible nature was already noted[5]. This conformation resembles the inward-facing, "locked" state of the WT[4,5] in the close packing observed between the transport domain and the trimerization scaffold (**Extended Data Fig. 7d**). Molecular dynamics (MD) simulations revealed that whereas Arg276 in the WT forms hydrogen bonds with Asp394 and bulk water molecules, the corresponding Arg395 in $H_{276,395}$-Glt_{Ph} faces the hydrophobic core of the bilayer. The resulting membrane remodeling is driven by the hydrophobic matching force[25,26], and is established by interactions of the Arg395 side chain with penetrating lipid phosphate groups and accompanying water molecules (**Extended Data Fig. 8**). Consequently, the penetrating polar moieties are positioned in an otherwise hydrophobic region of $H_{276,395}$-Glt_{Ph}, which can destabilize the inward-facing, locked conformation and increase water accessibility to the substrate-binding site and to the domain interface (**Fig. 5b**).

In protomers B and C the transport domains undergo identical and more dramatic changes (**Fig. 5a**), each swinging away from the trimerization scaffold by about 12° compared to "locked" protomer A. Consequently, a large crevice opens between HP2 and the scaffold, reducing the interface between the transport and scaffold domains from ~1300 $Å^2$ to ~900

Å^2 and allowing access to water, detergent or lipid molecules (**Fig. 5c**). This unusual, apparently "unlocked", conformation was observed in two protomers occupying distinct crystal packing environments and therefore seems to be determined by the properties of the protein itself and not by crystal contacts. The crevice it generates is largely hydrophobic, and closes rapidly in MD simulations when solvated only by water (**Extended Data Fig. 9a-c**). In contrast, the open interface between transport and trimerization domains is stable with lipids positioned in this space (**Extended Data Fig. 9 d-g**), suggesting that solvation by lipid or detergent molecules, is necessary. Notably, this crevice may allow HP2, whose gating role in the outward-facing state is well-established[3,6], to open when the transport domain is inward facing (**Fig. 5c**). If so, the substrate release might be facilitated in the unlocked conformation, a notion compatible with the markedly reduced substrate affinity of this mutant.

Discussion

Conformational transitions between outward- and inward-facing states are key events in transport cycles of secondary active transporters[27,28]. In glutamate transporters and possibly other families[29-31], such transitions involve elevator-like movements of the substrate-binding domains supported by relatively rigid scaffold domains. The frequency of such transitions in Glt_{Ph} in lipid bilayers and in the presence of physiological ionic gradients parallels the turnover rate of substrate uptake. This relationship also holds in a gain-of-function mutant $H_{276,395}$-Glt_{Ph} that exhibits a 1000-fold decreased substrate affinity and a 4-fold faster uptake rate. Collectively, our observations establish a direct correlation between the transport domain movements and substrate transport, and suggest an inverse relationship between substrate affinity and transport domain motions. The $H_{276,395}$-Glt_{Ph} mutant is special in this regard as other point mutations impact dynamics only and do not potentiate transport[9].

Importantly, the observed dynamic signatures strongly suggest that the rate-limiting step in this process is the unlocking of the transport domain from the trimerization scaffold (**Fig. 6a**). While both the WT and the $H_{276,395}$-Glt_{Ph} proteins exhibit similar transport domain structures and translocate similarly positioned charged groups (including Arg276 in the WT and Arg395 in the mutant), locked states are relatively unstable in the $H_{276,395}$-Glt_{Ph} mutant, leading to overall faster dynamics and uptake.

The locked and unlocked configurations of WT Glt_{Ph}, corresponding to quiescent and dynamic periods, respectively, coexist and interconvert spontaneously, which suggests that outward- and inward-facing states of Glt_{Ph} –and by extension EAATs –should be viewed as structurally heterogeneous ensembles. Increased quiescent period durations in the presence of substrate further suggest that ligand binding is allosterically coupled to the formation of locked states[9]. Based on these insights, we propose a simplified kinetic framework for the transport cycle that recapitulates the most salient experimentally observed features (**Fig. 6b, Extended Data Fig. 10**). The specific relationship of crystallographic snapshots of Glt_{Ph} and related proteins to the topological features of this framework will need to be examined carefully.

The structure of $H_{276,395}$-Glt_{Ph} (**Fig. 6c**) captures an unlocked configuration that appears relevant to the proposed transport cycle and uniquely suitable for ligand binding and release. While the molecular basis of how the mutations in $H_{276,395}$-Glt_{Ph} impact the locked-unlocked isomerization requires further investigation, MD simulations suggest that protein-lipid interactions are pivotal (**Extended Data Fig. 9**). The proposed role for the lipid hydrophobic tails in facilitating domain unlocking complements previous hypotheses that transient interface hydration facilitates transport domain translocation[5,14].

That two closely related Glt_{Ph} isoforms exhibit distinct kinetic and structural signatures foreshadows the possibility that human EAATs differ substantially from Glt_{Ph}, especially in their dynamic properties. Probing EAATs directly is therefore essential, particularly since the extent to which they might be diverted to kinetically stable, potentially off-pathway states may represent a regulatory modality.

METHODS

DNA manipulations, protein expression, purification and labeling

Single cysteine mutations were introduced by site-directed mutagenesis (Strategene) of a cysteine-less Glt_{Ph} background, in which seven non-conserved residues had been replaced with histidines resulting in improved expression levels (termed Glt_{Ph} from hereon for brevity)[3]. Constructs were verified by DNA sequencing and transformed into *E. coli* DH10-B cells (Invitrogen). Proteins were expressed as C-terminal $(His)_8$ fusions as described previously[2]. Briefly, isolated cell membranes were re-suspended in Buffer A, containing 20 mM Hepes/NaOH, pH 7.4, 200 mM NaCl, 0.1 mM L-aspartate, 0.1 mM Tris(2-carboxyethyl)phosphine (TCEP). Membranes were solubilized in the presence of 40 mM *n*-dodecyl β-D-maltopyranoside (DDM) for 1 hour at 4°C. Solubilized transporters were purified by metal-affinity chromatography in Buffer A supplemented with 1 mM DDM and eluted in 250 mM imidazole. The $(His)_8$-tag was cleaved by thrombin and proteins were further purified by size exclusion chromatography (SEC). For smFRET experiments, protein samples at 40 μM were labeled with a mixture of maleimide-activated Cy3 and Cy5 dyes that exhibit enhanced photostability[17,32] as well as biotin-PEG_{11}, at concentrations of 50, 100 and 25 μM, respectively, for 30 minutes at room temperature. Labeled proteins were purified away from the excess reagents by size exclusion chromatography. Their purity and specificity of labeling were assessed by SDS PAGE, which was followed by fluorescence imaging and Coomassie staining.

Protein reconstitution into liposomes for smFRET analysis and transport assays

Labeled and unlabeled Glt_{Ph} variants were reconstituted into liposomes as previouslydescribed[4,11]. Briefly, liposomes, prepared from 3:1 (w/w) mixture of *E. coli* total lipid extract and egg yolk phosphotidylcholine (Avanti Polar Lipids) in a buffer containing 20 mM Tris/HEPES, pH 7.4 and 100 mM KCl, were destabilized by addition of Triton X-100 at a detergent to lipid ratio of 0.5:1 (w/w). For reconstitution, proteins were added to lipids at final protein to lipid ratio of 1:1000 (w/w) and incubated for 30 minutes at room temperature. Detergents were removed by repeated incubations with Biobeads as described[11]. For smFRET and radioactive substrate uptake experiments, the same

proteoliposomes were extruded through 100 nm and 400 nm filters, respectively. This reconstitution strategy yields at most 1 and 16 Glt_{Ph} trimers per vesicle, respectively. Radioactive substrate uptake was measured as previously described[7]. Briefly, proteoliposomes were diluted into reaction buffer containing 20 mM Tris/HEPES, pH 7.4, 100 mM NaCl and 0.3 μM [^{3}H] L-aspartate at room temperature. Aliquots were removed at appropriate times, diluted in ice-cold quenching buffer (20 mM Tris/HEPES, pH 7.4, 100 mM LiCl) and filtered through 0.22 μm filters (Millipore). Protein concentration was estimated by the absorbance at 280 nm after correcting for the fluorophore contributions to the value. The amount of substrate uptake was normalized per mole of Glt_{Ph} monomers.

smFRET experiments

All experiments were performed using a home-built, prism-based total internal reflection fluorescence microscope constructed around a Nikon TE2000 Eclipse inverted microscope body using streptavidin-coated, passivated microfluidic imaging chambers[33]. Except when stated otherwise, labeled proteins (either detergent solubilized or liposome-reconstituted) were surface-immobilized via a biotin-streptavidin bridge. Except when stated otherwise, imaging experiments were performed in a buffer containing: 20 mM Hepes/Tris (pH 7.4), 5 mM BME, an enzymatic oxygen scavenger system comprising 1 unit/ml glucose oxidase (Sigma), 8 units/ml catalase (Sigma) and 0.1% glucose[34]. In addition, apo-Glt_{Ph} experiments included 200 mM KCl, Na^+/Asp-bound experiments included 200 mM NaCl and 0.1 mM aspartate and Na^+/TBOA-bound experiments included 200 mM NaCl, 10 mM TBOA. For experiments in detergent micelles, the buffers were also supplemented with 1 mM DDM. For imaging under transport conditions, the experiments were initiated in the absence of substrates (apo condition) on both sides of the membrane and chemical gradients were established by rapidly exchanging the proteoliposomes into an uptake buffer containing 100 mM NaCl and 100 μM aspartate. All data were collected at an imaging rate of 10 s^{-1} (100 ms integration time), except when otherwise stated. Fluorescence trajectories were selected for analysis using custom-made software implemented in Matlab (Mathworks) according to the following criteria[30]: a single catastrophic photobleaching event; over 8:1 signal-to-background noise ratio; a FRET lifetime of at least 5 seconds. FRET trajectories were calculated from the acquired intensities, I_{Cy3} and I_{Cy5}, using the formula FRET = $I_{Cy5}/(I_{Cy3} + I_{Cy5})$. Population contour plots were constructed by superimposing the FRET data from individual traces. Histograms of these population data were fit to Gaussian functions in Origin (OriginLab). The relative populations and dwell time distributions of each FRET state, as well as the transition frequencies between them, were obtained by idealizing the smFRET traces using QuB[35]. Transition density plots and the dwell time survival plots were plotted and fitted as described previously[13]. The logarithmic histograms of the dwell times were fitted to transformed probability density functions[9]. Over 300 molecules are included in each smFRET experiment to ensure that the experimental margin of error in the mean value of each distinct FRET state across the three experiments is less than 5%.

Crystallography

The R276S/M395R Glt_{Ph} mutant was purified by SEC in buffer containing 10 mM Tris/HEPES, pH 7.4, 100 mM NaCl and 7 mM n-decyl-β-D-maltopyranoside (DM). Protein solution at 3.5 mg/ml was mixed at 1:1 (vol.:vol.) ratio with the reservoir solution,

containing 50 mM sodium acetate, pH 5.6-6, 18–20 % PEG 400 and 100-150 mM magnesium acetate, and crystallized at 4° C by hanging-drop vapor diffusion. Crystals were cryoprotected in reservoir solution. Diffraction data were collected at National Synchrotron Light Source beamline X29. Diffraction data were indexed, integrated and scaled using the HKL2000 package[36]. Anisotropy correction was applied as described previously[5]. Further analyses were performed using CCP4 programs[37]. Initial phases were determined by molecular replacement in Phaser[38] using transport and trimeric scaffold domains as separate search models. The model was optimized by rounds of manual rebuilding in Coot[39] and refinement in Refmac5[40] with TLS[37]. During refinement, strict non-crystallographic three-fold symmetry constraints were applied to the three transport domains and to regions of the scaffold domain that are involved in trimerization interactions. In addition, strict two-fold symmetry constrains were applied to the entire B and C protomers, which exhibited identical positions of the transport domain. For the outward- and inward-facing states, published coordinates were used: accession number 2NWX[3] and 3KBC[4], respectively. For the open conformation of HP2 the accession number of the coordinates is 4OYF[6]. All structural renderings were generated using PyMol[41].

DEER measurements and data analysis

Measurements were performed at 60 K using a 17.3 GHz home-built Ku-band pulse spectrometer[42]. A standard four-pulse DEER sequence with π/2-π-π pulse widths of 16 ns, 32 ns and 32 ns, respectively, and a 32 ns π pump pulse was used routinely. The frequency separation between detection and pump pulses was 70 MHz. The detection pulses were positioned at the low-field edge of the nitroxide spectrum. The homogeneous background was removed from the raw time-domain signals and the distances were reconstructed from the baseline-corrected and normalized signals by using Tikhonov regularization method[43] and refined by maximum entropy method[44].

Molecular modeling

Molecular dynamics simulations using the Charmm27 force field (FF)[45] and updated lipid FF[46] were prepared as described previously[14] and run using the NAMD 2.9[47] software at 300K with PME electrostatics and standard parameters for the Charmm FF. Atomic coordinates for the inward-facing wild-type Glt_{Ph} were taken from PDB entry 3KBC[4] Simulations with the Gromos 54a7 FF[48] were prepared using the LAMBADA / InflateGRO membrane-embedding protocol[49] and run with the Gromacs 4.6.1[50] simulation package with reaction-field electrostatics and standard cutoffs for the Gromos FF. All simulations included pure POPC membranes, except Charmm27 Trajectory 3 (**Extended Data Fig. 9**), which contained a mixture of 18% POPC, 52% POPE, and 30% POPG (prepared with Charmm-GUI web-tool[51]), more similar to the composition of the liposomes used in experiments. In selected simulations **(Extended Data Fig. 9**), backbone C-α atoms were subjected to harmonic restraint potentials centered on positions from the X-ray structure with a harmonic constant of 0.1 kcal/mol$Å^2$ (NAMD) or 0.24 kcal/mol$Å^2$ (Gromacs). Docking of detergent and POPC lipid molecules was performed with Autodock Vina[52] within the Chimera 1.8 visualization software[53]. Lipid insertion in Charmm27 Trajectory 3 was performed as follows: (i) a frame from the molecular dynamics trajectory after 48ns of simulation time was selected; (ii) several lipid molecules restricted to various regions of the

interfaces in protomers A and C were docked, ignoring the water; (iii) docking poses among the highest ranked from all docking runs were combined, such that lipid molecules fill the available hydrophobic pockets without clashing with each other, and overlapping water molecules were discarded; (iv) locally minimization was performed with the Charmm27 force field, including solvent and side chains within 5 Å of inserted lipids; (v) the molecular dynamics simulation was restarted at 300K. Data processing and plots were performed in Matlab (Mathworks).

Kinetic simulations of smFRET data

For the simulations, we assumed that protomer motions are independent. The model presented in **Fig. 6** was employed to simulate the motions of individual protomers between outward- and inward-facing orientations in QuB[35]. The time-dependent configurations of two protomers were then assigned to FRET states as described (**Extended Data Fig. 3**). FRET traces were generated at 100 ms time-resolution in Matlab (Mathworks) using a Gaussian distribution of FRET efficiency values and widths derived from our experimental data. Initial estimates of the kinetic parameters were based on exponential fits of the experimental dwell time distributions (**Extended Data Table 1c**). The parameters were then manually optimized to recapitulate the experimental observables[20]: population FRET histograms, TDPs and the dwell-time histograms (**Extended Data Fig. 10**).

Extended Data

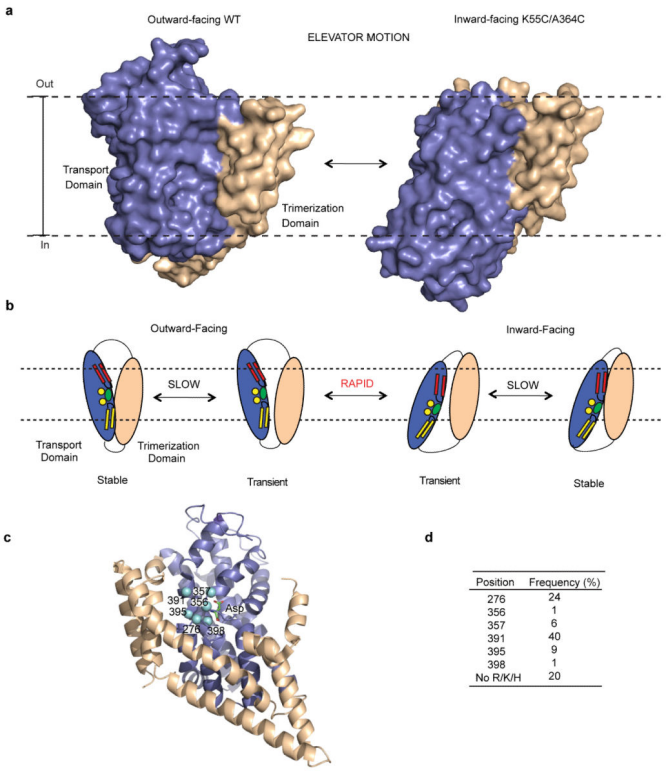

Extended Data Figure 1. Elevator model of transport and spatial conservation of a positively charged residue in glutamate transporter family

a, Glt_{Ph} protomers in the outward- (left) and inward-facing (right) conformation are shown in surface representation and viewed in membrane plane. Dashed lines represent an approximate position of the membrane hydrocarbon layer. In the inward-facing state, the transport domain (blue) is moved by ~15 Å across the bilayer relative to the trimerization domain (wheat). **b,** Schematic representation of dynamic mode-switching between stable and transient conformations. **c,** A single Glt_{Ph} protomer is shown in cartoon representation. Cyan balls emphasize the amino acid positions at which potentially positively charged residues occur in glutamate transporter homologues. **d,** Occurrence frequencies of these residues at the marked positions (Glt_{Ph} numbering). To obtain the frequencies, sequences were harvested from the PFAM database[54] (accession code PF00375). Sequences were parsed to exclude those with over 70 % identity and aligned using Clustal Omega[55].

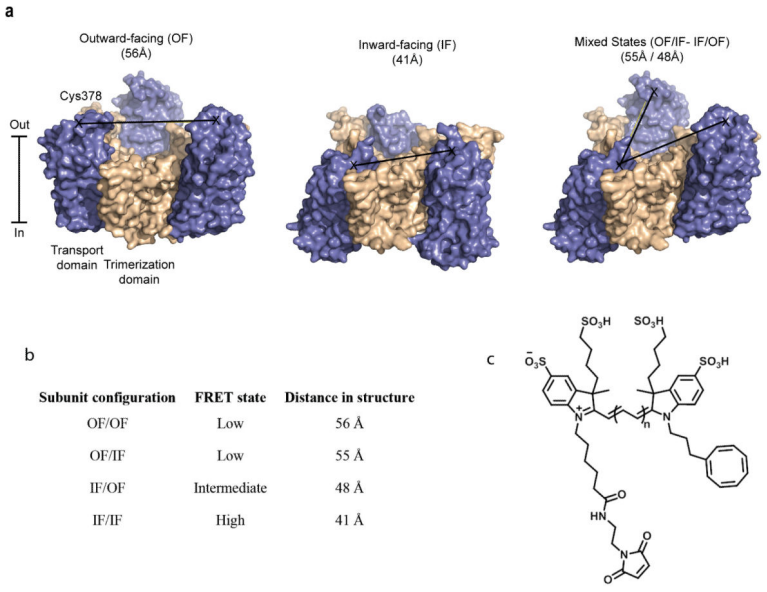

Subunit configuration	FRET state	Distance in structure
OF/OF	Low	56 Å
OF/IF	Low	55 Å
IF/OF	Intermediate	48 Å
IF/IF	High	41 Å

Extended Data Figure 2. Assignment of FRET efficiency states

a, Shown are the crystal structures of Glt_{Ph} trimers in symmetrical outward- (OF) and inward- (IF) facing states and a model of an asymmetric configuration with two outward- and one inward-facing protomers[2,4]. The structures are shown in surface representation and colored as in Extended Data Figure 1. Black lines connect Cα atoms of residue 378, and the corresponding distances are indicated above the structures. **b,** Expected FRET efficiency levels for these distances for all possible configurations of subunit pairs: outward/outward (OF/OF), outward/inward (OF/IF), inward/outward (IF/OF) and inward/inward (IF/IF)[4]. **c,** Intramolecularly stabilized 4S(COT)-maleimide Cy3 (n=1) and Cy5 (n=2) fluorophores used in this study synthesized as described previously[17,18] with the addition of two sulfonate groups for increased solubility.

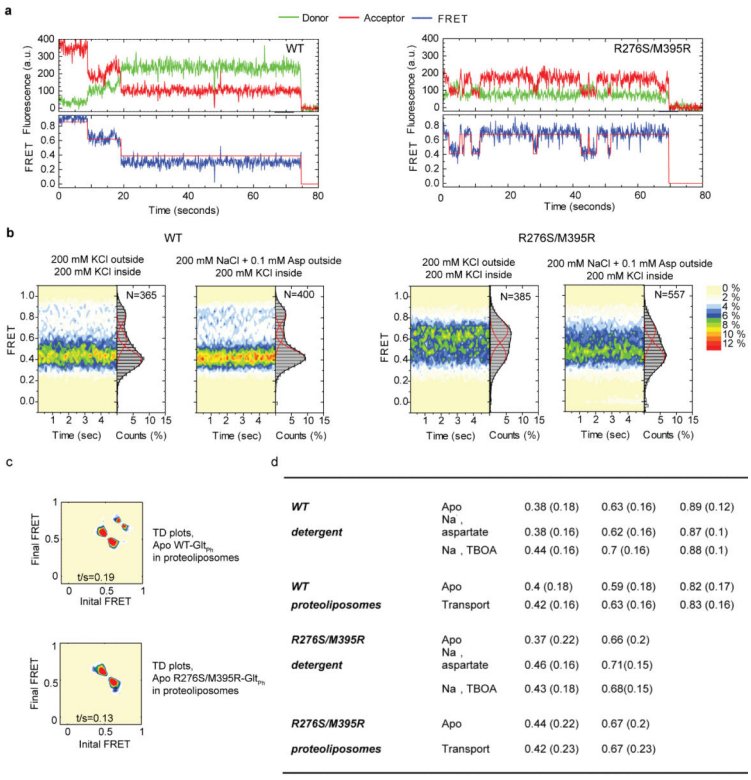

Extended Data Figure 3. Conformational state distributions of WT and $H_{276,395}$-Glt_{Ph} in proteoliposomes

a, Examples of smFRET recordings. Top panels show raw fluorescent signals originating from donor (green) and acceptor (red) dyes. Bottom panels show changes of FRET efficiency calculated from raw data (blue). Red solid lines through the data are idealizations obtained using QuB software[35] **b,** Contour plots and one-dimensional population histograms in the absence and presence of Na^+ and aspartate in the external liposome buffers. Buffer compositions inside and outside of the vesicles are shown above the panels. WT and $H_{276,395}$-Glt_{Ph} histograms are fitted to three and two Gaussian functions, respectively. **c,** Transitions density (TD) plots for the WT (left) and $H_{276,395}$-Glt_{Ph} (right) in proteoliposomes in the absence of Na^+ and aspartate in the external buffer. **d,** Means and widths (in brackets) of FRET efficiency distributions derived from Gaussian fits to proteoliposome data in comparison to detergent data.

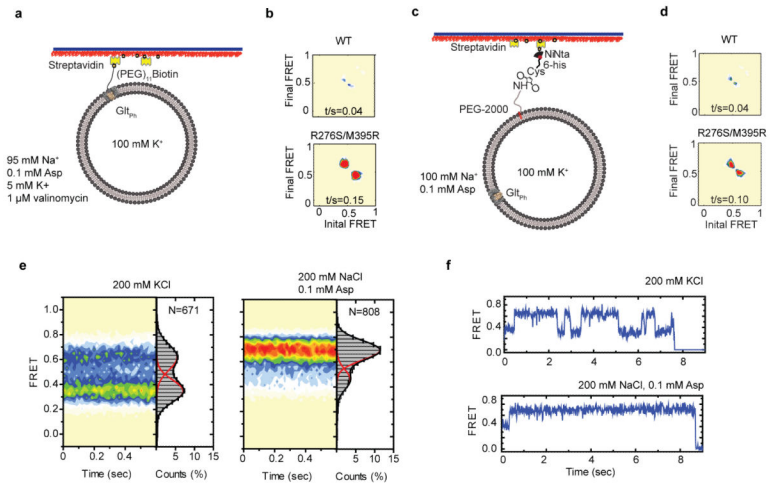

Extended Data Figure 4. Single-molecule dynamics using different liposome-attachment strategies and with higher time-resolution

a-d, Dynamic properties of $H_{276,395}$-Glt_{Ph} under transport conditions using a different surface-immobilization strategy and in the presence of electrical potential. a, Surface-immobilization strategy for proteoliposomes using His-tagged lipids. **b,** Transition frequencies for WT (top) and $H_{276,395}$-GltPh (bottom) trimers reconstituted into his-tagged liposomes that were site-specifically labeled in just two protomers with intramolecularly photostabilized Cy3 and Cy5 fluorophores. **c,** A negative inside voltage potential was established in proteoliposomes by adding valinomycin to the uptake buffer. **d,** Transition frequencies for WT (top) and $H_{276,395}$-GltPh (bottom) in the presence of valinomycin. Each experiment shown includes statistics based on > 250 individual molecules. The standard error in transition frequency measurements is approximately 0.015 s^{-1}. **e-f,** Dynamic properties of $H_{276,395}$-Glt_{Ph} probed at 15 ms time resolution. Contour plots and one-dimensional population FRET efficiency histograms (e) observed for the humanized mutant in detergent solution in the absence (left) and presence (right) of 100 mM NaCl and 100 µM aspartate. Examples of single-molecule trajectories (f).

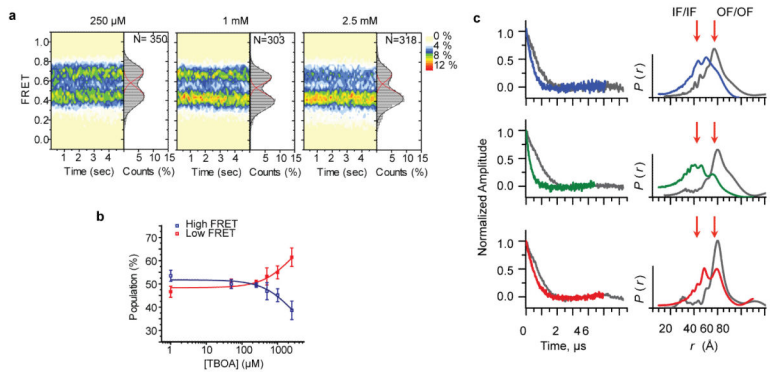

Extended Data Figure 5. Population changes in response to ligand binding

a-b, TBOA binding to $H_{276,395}$-Glt_{Ph} measured in smFRET experiments. Contour plots and population FRET efficiency histograms in the presence of increasing concentrations of TBOA (**a**). Changes in low- (red) and high- (blue) FRET state populations as a function of

TBOA concentration (**b**). Solid lines through the data correspond to the Hill equation $y = y_{min} + (y_{max}-y_{min})(x^n/(x^n+K_D^n))$ with K_D=2.4 mM and n=1. The data points shown are averages and standard errors from three independent biological replicates. **c,** Experimental time domain DEER data (left) and reconstructed distance distributions (right) for $H_{276,395}$-Glt_{Ph} (shown in colors) and WT transporter (black) spin-labeled on residue Cys378 in detergent solution. The data were collected in the absence of ligands (top), in the presence of 100 mM Na^+ and 350 μM aspartate (middle) and in the presence of 100 mM Na^+ and 480 μM TBOA (bottom). The red arrows above the distance distributions mark distances between residues 378 extracted from crystal structures of the symmetric outward- (OF/OF) and inward- (IF/IF) facing states. The data for the WT transporter were adapted from a published study[11]. Notably, the data show that in the apo transporter, outward- and inward-facing states are similarly populated. Binding of Na^+ ions and aspartate favors the inward-facing state, while binding of TBOA favors the outward-facing state.

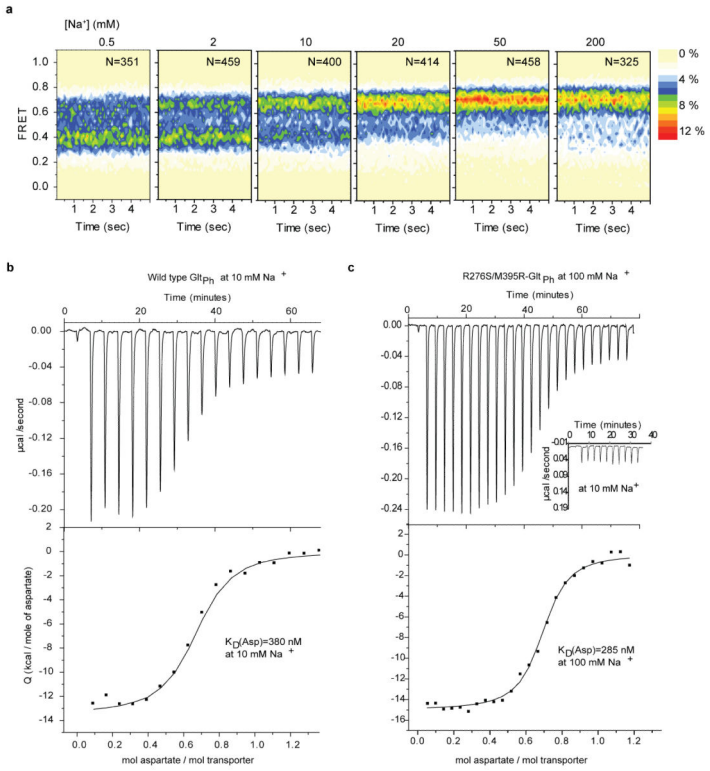

Extended Data Figure 6. Aspartate binding experiments

a, FRET efficiency population contour plots determined for $H_{276,395}$-Glt_{Ph} in detergent micelles in the presence of 100 μM aspartate and increasing concentrations of Na^+ ions (indicated above the panels). **b-c,** Representative aspartate binding isotherms derived from ITC experiments for the WT Glt_{Ph} (**b**) and $H_{276,395}$-Glt_{Ph} (**c**) in the presence of 10 mM Na^+ and 100 mM Na^+, respectively. Notably, the binding of aspartate to $H_{276,395}$-Glt_{Ph} in the presence of 10 mM Na^+ is too weak to measure (inset). Binding experiments were performed using small-volume Nano ITC (*TA Instruments*). Upper panels show raw data. The cell contained 30 μM (WT-Glt_{Ph}) and 40 μM (H- Glt_{Ph}) protein buffer containing 20 mM HEPES/Tris, pH 7.4 and 0.1 mM DDM and indicated concentrations of NaCl. The

syringe contained Asp at 200 μM concentration in the same buffer; every injection contained 5 μl. Data were processed and analyzed using manufacturer's software (lower panels). Solid lines through the data are fits to independent binding sites model with the following K_D, enthalpy (ΔH), and apparent number of binding sites (n): 380 nM, 15 kcal/mol and 0.65 for the WT transporter, and 285 nM, 16 kcal/mol and 0.68 for $H_{276,395}$-Glt_{Ph}.

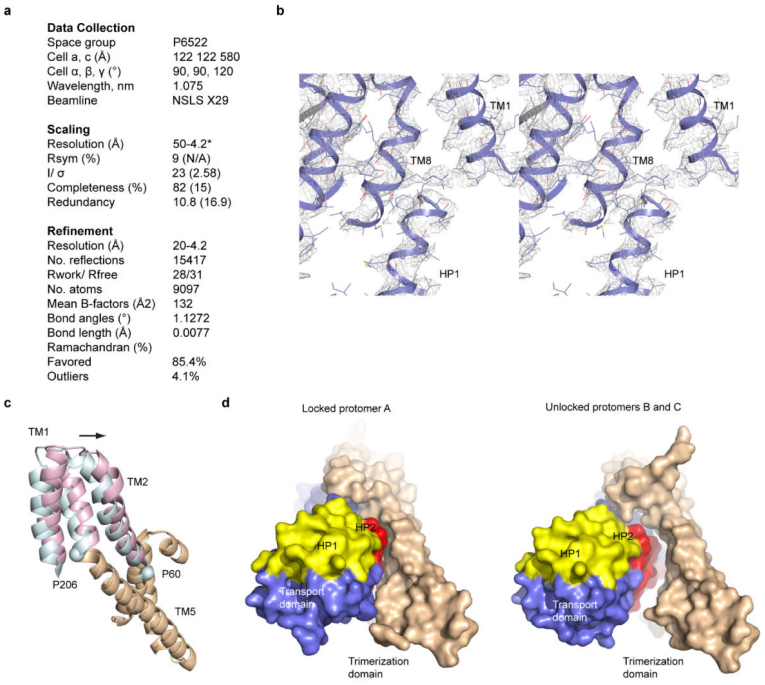

Extended Data Figure 7. Data collection and refinement for Na^+ and aspartate bound R276S/M395R-Glt_{Ph}

a, Table showing data collection and refinement statistics. Scaling and refinement statistics were obtained after anisotropy correction by ellipsoidal truncation using high-resolution cutoffs of 4.9 Å along the *a* and *b* axis, and of 4.2 Å along the c axis. **b,** Stereoview of the $2F_o$-F_c electron density map for $H_{276,395}$-Glt_{Ph} contoured at 1.5 σ around residue Arg395 in unlocked protomer C. Protein backbone (maroon) is shown in cartoon representations and side chains are shown as lines and colored by atom type. **c,** Superimposed scaffold domains of the inward-facing WT and $H_{276,395}$-Glt_{Ph} are shown in cartoon representation. The labile portions are colored cyan (WT) and magenta (mutant). Helices bend at conserved Pro60 and Pro206 residues (spheres). **d,** Locked (left) and unlocked (right) mutant protomers viewed from the cytoplasm and shown in surface representation.

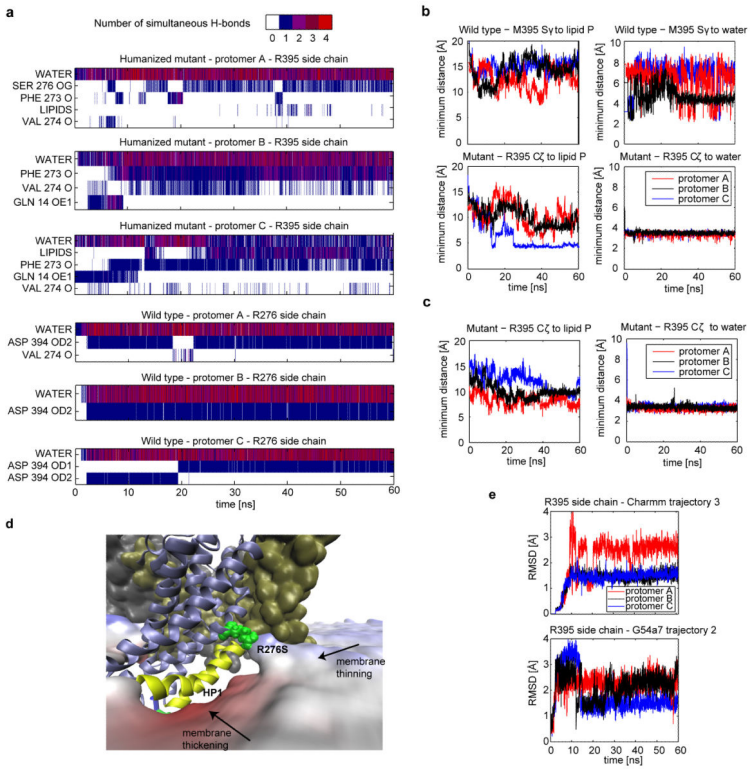

Extended Data Figure 8. Arg395 adapts to its environment

a, The arginine side chain (Arg276 in the WT; Arg395 in $H_{276,395}$-Glt_{Ph}) is seen in MD simulations to engage in hydrogen bonding interactions. Shown is the extent of the hydrogen bonds formation as a function of simulation time in Charmm Trajectory 3 (see Extended Data Figure 10). The main interactions of the arginine in both mutant and WT are with water molecules, but the locations of the waters are very different. In $H_{276,395}$-Glt_{Ph}, Arg395 side chain is located 5 to 9 Å below the level of the membrane surface, so that the water molecules are those penetrating the membrane-protein interface due to remodeling the membrane. In the WT, the water molecules interacting with Arg276 are in the space created inside the protein. **b**, The minimum distance from WT Met395 (top) or mutant Arg395 (bottom) side chains to any lipid phosphate group (left) or any water molecule (right) in Charmm Trajectory 3. In $H_{276,395}$-Glt_{Ph} after the initial equilibration phase, lipid phosphate groups interact with Arg395 either directly (5 Å distance) or through water (7.5 Å distance). In the WT, lipid head groups remain far from the hydrophobic Met395 side chain. Water interacts constantly with Arg395, but only occasionally with Met395 (in protomer B, a water molecule approaches M395 from the inside of the protein, at the interface between transport and trimerization domains). **c**, The same set of distances as in (b) for the mutant, from a different trajectory (G54a7 Trajectory 2) obtained independently, utilizing a different force field. The same trends are observed as in (b), showing proximity to the polar environment. **d**, Membrane bending (blue indicates thinning, red indicates thickening) close to Arg395 (green) which exposes its side chain to a polar environment comprised of water molecules and lipid head groups. **e**, RMSD of the Arg395 side chain with respect to the crystal structure after alignment on the trimerization domain, calculated from Charmm Trajectory 3

and G54a7 Trajectory 2. The side chain initially samples different conformations before settling into the membrane-exposed position shown in panel (d).

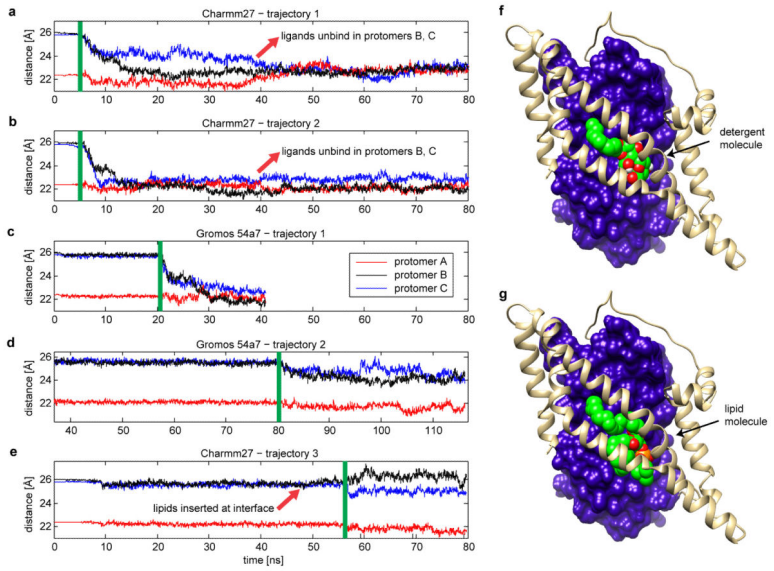

Extended Data Figure 9. Lipids or detergent molecules stabilize the unlocked conformation of $H_{276,395}$-Glt_{Ph}

a-e, Center-of-mass distance between the transport and scaffold domains of protomers A, B, and C of $H_{276,395}$-Glt_{Ph} as a function of MD simulation time.. The data are from five independent simulations initiated with position restraints on the Cα atoms (later released at different time points) and with the domain interface solvated with water. The vertical green lines indicate the moment in the corresponding trajectory when position restraints were turned off. Panels **a** and **b** show two repeats of the same starting structure simulated with the Charmm force field[45] and panel **c** with Gromos force field[48]. The transport domains in protomers B and C collapse onto the trimerization domain rapidly and loose their ligands in some cases (red arrows). **d**, A simulation, in which lipid tails partially insert into the interface spontaneously; the unlocked structure is stable much longer (note the different time scales on the time axis), and the collapse is only partial. **e,** The trajectory of a NAMD simulation (Charmm force field) in which lipid molecules were docked into the interface of protomers B and C at the time marked by the red arrow (3 lipids per protomer). The lipids remained in the docked region for the entire duration of the simulation and stabilized the position of the transport domain. **f** and **g**, The best scored docking poses for a detergent molecule and a POPC lipid, respectively, docked at the interface of protomer C.

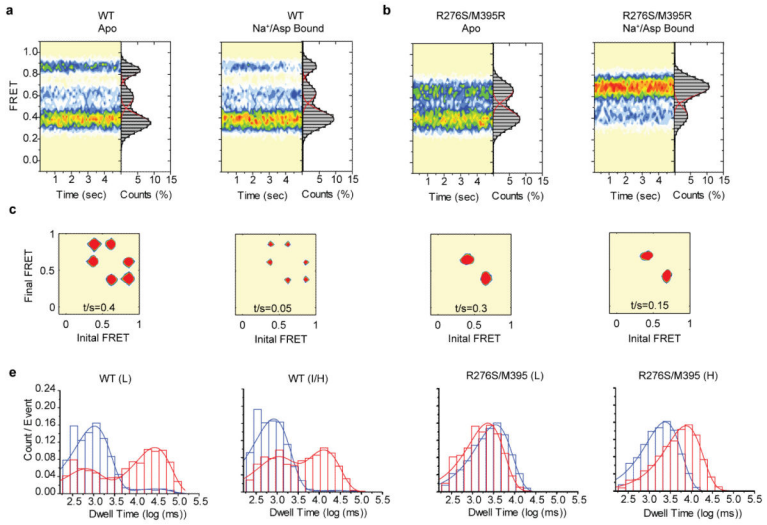

Extended Data Figure 10. Simulated smFRET data recapitulate experimental observations

a-d, Simulated FRET efficiency population contour plots (left side of each panel) and cumulative population histograms (right side) for WT Glt_{Ph} (**a**) and $H_{276,395}$-Glt_{Ph} (**b**), and the corresponding transition density plots (**c** and **d**), (see **Fig. 2** for corresponding experimental data). As noted before[9], there are fewer transitions observed between the low- and high-FRET states in the WT transporter than would be expected from the model. This may either be because the model does not recapitulate the noise correctly or it may reflect previously uncharacterized communication between the protomers that warrants further investigation. **e-f,** Dwell time distributions for the low- (left panel) and intermediate- and high-FRET states (right panels) obtained for WT Glt_{Ph} (**e**) and $H_{276,395}$- Glt_{Ph} (**f**) (see **Fig. 4** for corresponding experimental data).

Extended Data Table 1

FRET state assignments and populations; time constants for the slow and fast components.

a, FRET State Population Distributions in proteoliposomes

WT Glt_{ph}

FRET	*Subunit configuration*	*Apo, %*	*P(out)=0.55, %*	*Transport, %*	*P(out)=0.65, %*
Low	OF/OF+OF/IF	54	55	63	65
Intermediate	IF/OF	27	25	22	22
High	IF/IF	19	20	15	13

R276S/M395R GIt_{ph}

FRET	*Subunit configuration*	*Apo, %*	*Transport, %*
Lower	OF/OF+OF/IF	40	55
Higher	IF/OF+IF/IF	60	45

b, FRET State Population Distributions in detergent micelles

WT GIt_{ph}

FRET	*Subunit configuration*	*Apo, %*	*P(out)=0.45, %*	*Bound, %*	*P(out)=0.5, %*
Low	OF/OF+OF/IF	46	45	49	50
Intermediate	IF/OF	24	25	25	25
High	IF/IF	29	30	24	**25**

R276S/M395R Glt_{ph}

FRET	*Subunit configuration*	*Apo, %*	*Transport, %*
Lower	OF/OF+OF/IF	62	30
Higher	IF/OF+IF/IF	38	70

c, Time constant for stable (slow) and transient (fast) FRET States in detergent micelles

WT	***Low FRET***		***Intermediate / High FRET***	
	$t_{Fast,}$ S	t_{Slow}, S	t_{Fast}, S	t_{Slow}, S
Apo	~ 0.6	~ 6	~ 0.6	~ 5
Na^+, aspartate	~ 0.7	~ 12	~ 0.7	~ 15
R276S/M395R	***Low FRET***		***Higher FRET***	
	t, s		**t, s**	
Apo	~ 1.5		~ 1.1	
Na^+, aspartate	~ 1.7		~ 7.6	

a-b, Shown are the assignments of FRET states to configurations of labeled subunit pairs and corresponding observed populations, rounded to integer numbers. Also shown are the calculated populations considering the probability of a protomer to be in the outward facing state *P(out)* and assuming independent protomers in the trimer. **c,** Time constants for the WT transporter, □□, of the slow and fast components were derived from fitting the survival data compiled from the measured dwell times to double exponential function. The time constants for the $H_{276,395}$-Glt_{Ph}mutant were obtained by fitting the survival data to a single exponential function. Shown are averages from three independent experiments. The standard errors are within 5%. Dwell times longer than 10 s are significantly underestimated because photobleaching, which occurs with time constant of ~40 s, is limiting the observation window.

Supplementary Material

Refer to Web version on PubMed Central for supplementary material.

Acknowledgements

Authors would like to thank Peter Borbat for help with DEER data collection; Hong Zhao for his help with fluorophore synthesis; Grégory Verdon, Gabriel Glenn Gregario and Secheol Oh for helpful discussions. The authors acknowledge the staff of X29 beamline at National Synchrotron Light Source and the computational resources at the Texas Advanced Computing Center at the University of Texas at Austin and the National Energy Research Scientific Computing Center, supported by the Office of Science of the U.S. Department of Energy under Contract No. DE-AC02-05CH11231. The work was supported in part by the National Institute of Health grants 5U54GM087519 (to OB and HW); P01DA012408 (to HW); R01GM098859 and R21MH099491 (to SCB); P41GM103521 and R010EB003150 (to JHF).

References

1. Zerangue N, Kavanaugh MP. Flux coupling in a neuronal glutamate transporter. Nature. 1996; 383:634–7. [PubMed: 8857541]
2. Yernool D, Boudker O, Jin Y, Gouaux E. Structure of a glutamate transporter homologue from Pyrococcus horikoshii. Nature. 2004; 431:811–8. [PubMed: 15483603]

3. Boudker O, Ryan RM, Yernool D, Shimamoto K, Gouaux E. Coupling substrate and ion binding to extracellular gate of a sodium-dependent aspartate transporter. Nature. 2007; 445:387–93. [PubMed: 17230192]
4. Reyes N, Ginter C, Boudker O. Transport mechanism of a bacterial homologue of glutamate transporters. Nature. 2009; 462:880–5. [PubMed: 19924125]
5. Verdon G, Boudker O. Crystal structure of an asymmetric trimer of a bacterial glutamate transporter homolog. Nat Struct Mol Biol. 2012; 19:355–7. [PubMed: 22343718]
6. Verdon G, Oh S, Serio RN, Boudker O. Coupled ion binding and structural transitions along the transport cycle of glutamate transporters. Elife. 2014; 3:e02283. [PubMed: 24842876]
7. Ryan RM, Compton EL, Mindell JA. Functional characterization of a Na+-dependent aspartate transporter from Pyrococcus horikoshii. J Biol Chem. 2009; 284:17540–8. [PubMed: 19380583]
8. Groeneveld M, Slotboom DJ. Na(+):aspartate coupling stoichiometry in the glutamate transporter homologue Glt(Ph). Biochemistry. 2010; 49:3511–3. [PubMed: 20349989]
9. Akyuz N, Altman R, Blanchard SC, Boudker O. Transport dynamics of a glutamate transporter homologue. Nature. 2013; 502:114–8. [PubMed: 23792560]
10. Erkens GB, Hanelt I, Goudsmits JM, Slotboom DJ, van Oijen AM. Unsynchronised subunit motion in single trimeric sodium-coupled aspartate transporters. Nature. 2013; 502:119–23. [PubMed: 24091978]
11. Georgieva ER, Borbat PP, Ginter C, Freed JH, Boudker O. Conformational ensemble of the sodium-coupled aspartate transporter. Nat Struct Mol Biol. 2013; 20:215–21. [PubMed: 23334289]
12. Hanelt I, Wunnicke D, Bordignon E, Steinhoff HJ, Slotboom DJ. Conformational heterogeneity of the aspartate transporter Glt(Ph). Nat Struct Mol Biol. 2013; 20:210–4. [PubMed: 23334291]
13. Zhao Y, et al. Single-molecule dynamics of gating in a neurotransmitter transporter homologue. Nature. 2010; 465:188–93. [PubMed: 20463731]
14. Stolzenberg S, Khelashvili G, Weinstein H. Structural Intermediates in a Model of the Substrate Translocation Path of the Bacterial Glutamate Transporter Homologue GltPh. J Phys Chem B. 2012; 116:5372–83. [PubMed: 22494242]
15. Ryan RM, Kortt NC, Sirivanta T, Vandenberg RJ. The position of an arginine residue influences substrate affinity and K+ coupling in the human glutamate transporter, EAAT1. J Neurochem. 2010; 114:565–75. [PubMed: 20477940]
16. Borre L, Kanner BI. Coupled, but not uncoupled, fluxes in a neuronal glutamate transporter can be activated by lithium ions. J Biol Chem. 2001; 276:40396–401. [PubMed: 11479303]
17. Altman RB, et al. Enhanced photostability of cyanine fluorophores across the visible spectrum. Nat Methods. 2012; 9:428–9. [PubMed: 22543373]
18. Zheng Q, et al. On the Mechanisms of Cyanine Fluorophore Photostabilization. J Phys Chem Lett. 2012; 3:2200–2203. [PubMed: 22984636]
19. Alejo JL, Blanchard SC, Andersen OS. Small-molecule photostabilizing agents are modifiers of lipid bilayer properties. Biophys J. 2013; 104:2410–8. [PubMed: 23746513]
20. Geggier P, et al. Conformational sampling of aminoacyl-tRNA during selection on the bacterial ribosome. J Mol Biol. 2010; 399:576–95. [PubMed: 20434456]
21. Grewer C, et al. Individual subunits of the glutamate transporter EAAC1 homotrimer function independently of each other. Biochemistry. 2005; 44:11913–23. [PubMed: 16128593]
22. Groeneveld M, Slotboom DJ. Rigidity of the subunit interfaces of the trimeric glutamate transporter GltT during translocation. J Mol Biol. 2007; 372:565–70. [PubMed: 17673229]
23. Reyes N, Oh S, Boudker O. Binding thermodynamics of a glutamate transporter homolog. Nat Struct Mol Biol. 2013; 20:634–40. [PubMed: 23563139]
24. Shimamoto K, et al. DL-threo-beta-benzyloxyaspartate, a potent blocker of excitatory amino acid transporters. Mol Pharmacol. 1998; 53:195–201. [PubMed: 9463476]
25. Mondal S, Khelashvili G, Shi L, Weinstein H. The cost of living in the membrane: a case study of hydrophobic mismatch for the multi-segment protein LeuT. Chemistry and physics of lipids. 2013; 169:27–38. [PubMed: 23376428]

26. Mondal S, Khelashvili G, Weinstein H. Not Just an Oil Slick: How the Energetics of Protein-Membrane Interactions Impacts the Function and Organization of Transmembrane Proteins. Biophysical Journal. 2014; 106:2305–2316. [PubMed: 24896109]
27. Jardetzky O. Simple allosteric model for membrane pumps. Nature. 1966; 211:969–70. [PubMed: 5968307]
28. Mitchell P. Translocations through natural membranes. Adv Enzymol Relat Areas Mol Biol. 1967; 29:33–87. [PubMed: 4235731]
29. Lee C, et al. A two-domain elevator mechanism for sodium/proton antiport. Nature. 2013; 501:573–7. [PubMed: 23995679]
30. Quistgaard EM, Low C, Moberg P, Tresaugues L, Nordlund P. Structural basis for substrate transport in the GLUT-homology family of monosaccharide transporters. Nat Struct Mol Biol. 2013; 20:766–8. [PubMed: 23624861]
31. Zhou X, et al. Structural basis of the alternating-access mechanism in a bile acid transporter. Nature. 2014; 505:569–73. [PubMed: 24317697]
32. Zheng Q, et al. Ultra-stable organic fluorophores for single-molecule research. Chem Soc Rev. 2014; 43:1044–56. [PubMed: 24177677]
33. Munro JB, Altman RB, O'Connor N, Blanchard SC. Identification of two distinct hybrid state intermediates on the ribosome. Mol Cell. 2007; 25:505–17. [PubMed: 17317624]
34. Dave R, Terry DS, Munro JB, Blanchard SC. Mitigating unwanted photophysical processes for improved single-molecule fluorescence imaging. Biophys J. 2009; 96:2371–81. [PubMed: 19289062]
35. Qin F. Restoration of single-channel currents using the segmental k-means method based on hidden Markov modeling. Biophys J. 2004; 86:1488–501. [PubMed: 14990476]
36. Otwinowski Z, Minor W. Processing of X-ray Diffraction Data Collected in Oscillation Mode. Methods in Enzymology. 1997; 276:307–326.
37. Collaborative Computational Project, N. The CCP4 suite: programs for protein crystallography. Acta Crystallogr D Biol Crystallogr. 1994; 50:760–3. [PubMed: 15299374]
38. McCoy AJ, et al. Phaser crystallographic software. J Appl Crystallogr. 2007; 40:658–674. [PubMed: 19461840]
39. Emsley P, Cowtan K. Coot: model-building tools for molecular graphics. Acta Crystallogr D Biol Crystallogr. 2004; 60:2126–32. [PubMed: 15572765]
40. Murshudov GN, et al. REFMAC5 for the refinement of macromolecular crystal structures. Acta Crystallogr D Biol Crystallogr. 2011; 67:355–67. [PubMed: 21460454]
41. The PyMOL Molecular Graphics System. Version 1.5.0.4 Schrödinger, LLC.
42. Borbat PP, Crepeau RH, Freed JH. Multifrequency two-dimensional Fourier transform ESR: an X/Ku-band spectrometer. J Magn Reson. 1997; 127:155–67. [PubMed: 9281479]
43. Chiang YW, Borbat PP, Freed JH. The determination of pair distance distributions by pulsed ESR using Tikhonov regularization. J Magn Reson. 2005; 172:279–95. [PubMed: 15649755]
44. Chiang YW, Borbat PP, Freed JH. Maximum entropy: a complement to Tikhonov regularization for determination of pair distance distributions by pulsed ESR. J Magn Reson. 2005; 177:184–96. [PubMed: 16137901]
45. MacKerell AD Jr, Feig M, Brooks III CL. Improved treatment of the protein backbone in empirical force fields. J. Am. Chem. Soc. 2004; 126:698–699. [PubMed: 14733527]
46. Klauda JB, et al. Update of the CHARMM all-atom additive force field for lipids: validation on six lipid types. The journal of physical chemistry B. 2010; 114:7830–7843. [PubMed: 20496934]
47. Phillips JC, et al. Scalable molecular dynamics with NAMD. Journal of computational chemistry. 2005; 26:1781–1802. [PubMed: 16222654]
48. Schmid N, et al. Definition and testing of the GROMOS force-field versions 54A7 and 54B7. European Biophysics Journal. 2011; 40:843–856. [PubMed: 21533652]
49. Schmidt TH, Kandt C. LAMBADA and InflateGRO2: Efficient membrane alignment and insertion of membrane proteins for molecular dynamics simulations. Journal of chemical information and modeling. 2012; 52:2657–2669. [PubMed: 22989154]

50. Pronk S, et al. GROMACS 4.5: a high-throughput and highly parallel open source molecular simulation toolkit. Bioinformatics. 2013; 29:845–854. [PubMed: 23407358]

51. Jo S, Kim T, Iyer VG, Im W. CHARMM-GUI: a web-based graphical user interface for CHARMM. J Comput Chem. 2008; 29:1859–65. [PubMed: 18351591]

52. Trott O, Olson AJ. AutoDock Vina: improving the speed and accuracy of docking with a new scoring function, efficient optimization, and multithreading. Journal of computational chemistry. 2010; 31:455–461. [PubMed: 19499576]

53. Pettersen EF, et al. UCSF Chimera -- a visualization system for exploratory research and analysis. J. Comput. Chem. 2004; 25:1605–1612. [PubMed: 15264254]

54. Finn RD, et al. Pfam: the protein families database. Nucleic Acids Res. 2014; 42:D222–30. [PubMed: 24288371]

55. Sievers F, et al. Fast, scalable generation of high-quality protein multiple sequence alignments using Clustal Omega. Mol Syst Biol. 2011; 7:539. [PubMed: 21988835]

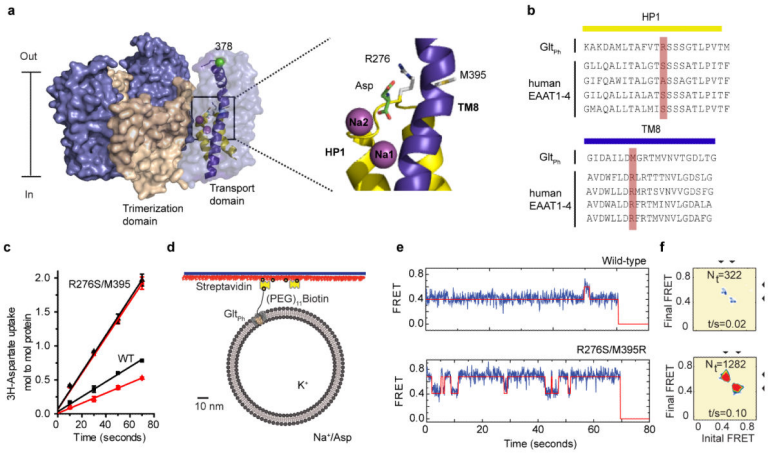

Figure 1. Transport rates and 'elevator-like' domain dynamics are correlated

a, Surface representation of the outward-facing Glt_{Ph} showing the transport (blue) and scaffold (wheat) domains. In one protomer, HP1 (yellow) and TM8 (dark blue) are emphasized as cartoons. In the enlarged substrate-binding site (right), mutated residues and aspartate are shown as sticks and ions as spheres. **b,** Sequence alignment for HP1 and TM8 with mutation sites highlighted in pink. **c,** Aspartate uptake by unlabeled (black) and labeled (red) transporters. Substrate uptake data are shown as averages of at least three experiments with standard deviations. **d,** Proteoliposome attachment strategy. **e,** smFRET trajectories recorded for the WT and mutant in proteoliposomes under transport conditions. **f**, Transition density plots corresponding to **e**. The average transition frequencies (*t/s*) and the number of total transitions (N_t) are shown. Color scale is from tan (lowest) to red (highest frequency).

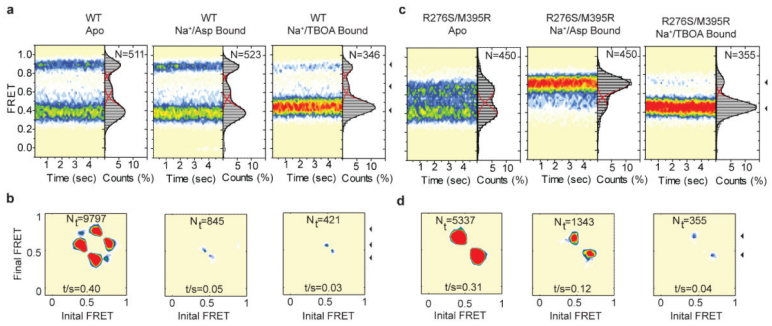

Figure 2. Ligand-dependent state distributions in detergent

In each panel, time-dependent FRET efficiency population contour plots (left) and cumulative population histograms (right) are shown for the WT (**a**) and mutant (**c**). Experimental conditions are indicated above the panels. Contour plots are color-coded from tan (lowest) to red (highest population);color scale from 0-12%. Histograms display the time-averaged state distributions. Solid black lines are fits to sums of individual Gaussian functions (red lines). *N* is the number of molecules analyzed. **e, d,** Corresponding transition density plots (as in Fig. 1).

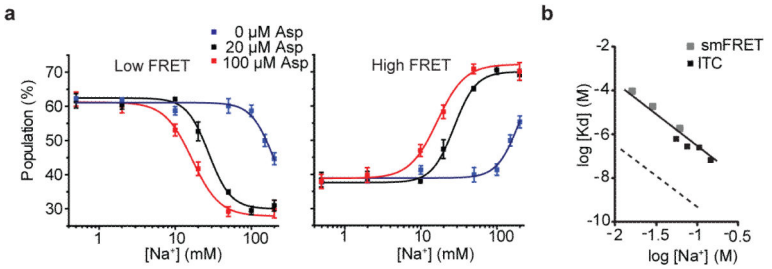

Figure 3. Coupled Na^+ and aspartate binding to $H_{276,395}$-Glt_{Ph}

a, Populations of low- (left) and higher- (right) FRET states determined for $H_{276,395}$-Glt_{Ph} in detergent micelles as functions of Na^+ concentration in the presence of 0 (blue), 20 (black) and 100 (red) μM aspartate. Solid lines are fits to Hill equation with K_D=200, 30 and 15 mM, respectively, and *n* value of 3. The data points shown are averages and standard errors from three independent biological replicates. **b,** Logarithmic plots of aspartate K_D-s as functions of Na^+ concentrations. Data are from ITC (black) and smFRET (gray). The solid line through the data is a linear fit with slope 3.2. The extent of coupling between Na^+ and aspartate binding is similar to WT (dashed line)[23].

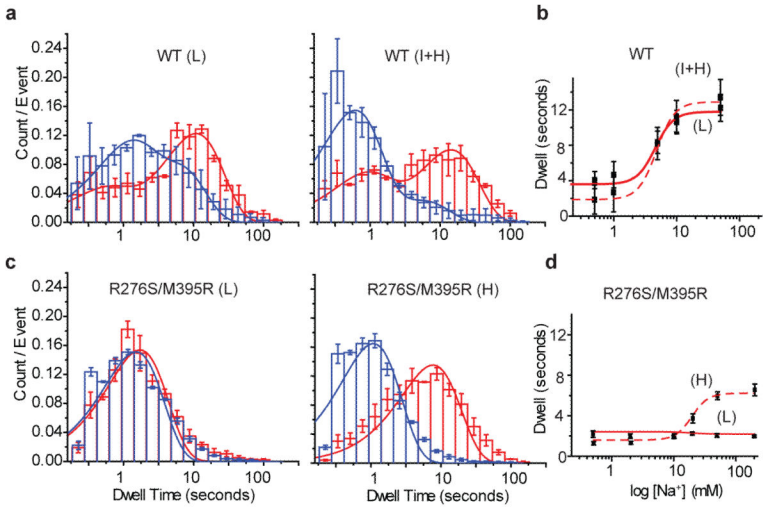

Figure 4. Monodisperse dynamic behavior of $H_{276,395}$-Glt_{Ph}

Dwell time distributions (**a, c**) and average dwell times (**b, d**) for the low- (L, solid lines) and intermediate- and high-FRET states (I+H, dashed lines) obtained for the WT (**a, b**) and $H_{276,395}$-Glt_{Ph} (**c, d**) in detergent. The distributions for apo (blue) and Na^+/aspartate-bound proteins (red) were fitted to a probability density function. The fitted time constants are in **Extended Data Table 1c**. Average dwells are plotted as functions of Na^+ concentration in the presence of 10 and 100 μM aspartate for WT and $H_{276,395}$-Glt_{Ph}, respectively. Solid lines are fits to Hill equation with K_D=15 mM and n= 3.2 for WT and $K_{D=}$ 19 mM and n=3.2 for $H_{276,395}$-Glt_{Ph}. The data points shown are averages and standard errors from three independent biological replicates.

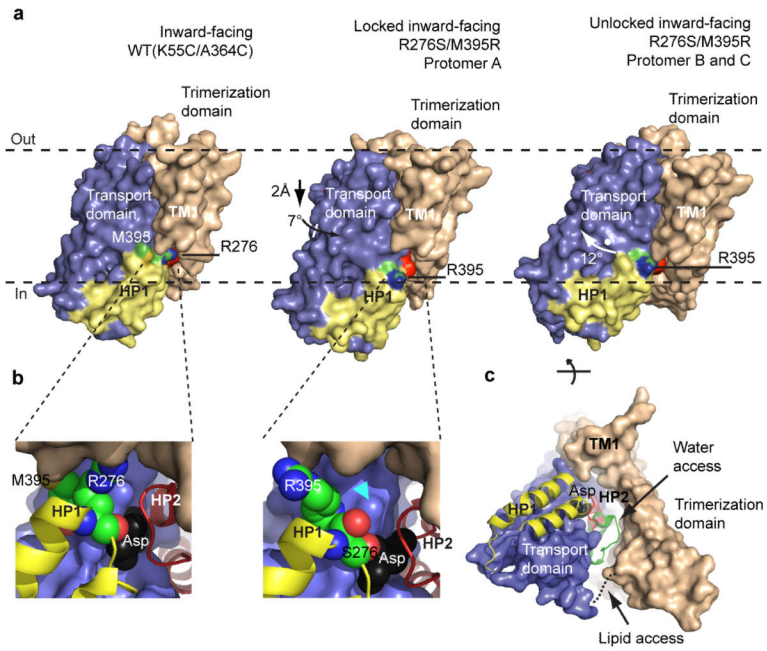

Figure 5. Crystal structure of the $H_{276,395}$-Glt_{Ph}

a, Single protomers of inward-facing WT (left), locked mutant (center) and unlocked mutant (right) in surface representation, colored as in Fig. 1,;HP2 is red. Residues 276 and 395 are colored by atom type. The approximate limits of the hydrocarbon layer of the membrane are shown as dashed lines. **b,** Substrate binding sites (enlarged) viewed from the cytoplasm. HP1 and HP2 are in cartoon representation; aspartate (black) and residues 276, 395 and Asp394 (colored by atom type) are emphasized as spheres. Arrowhead (cyan) marks the region of increased solvent accessibility. **e**, Cytoplasmic view of the unlocked protomer showing the crevice at the domain interface. Dashed line replaces TM2-TM3 loop for clarity. Arrows indicate regions of increased water and lipid accessibility. Open conformations of HP2 were modeled based on the TBOA-bound (green) structure of Glt_{Ph}[3].

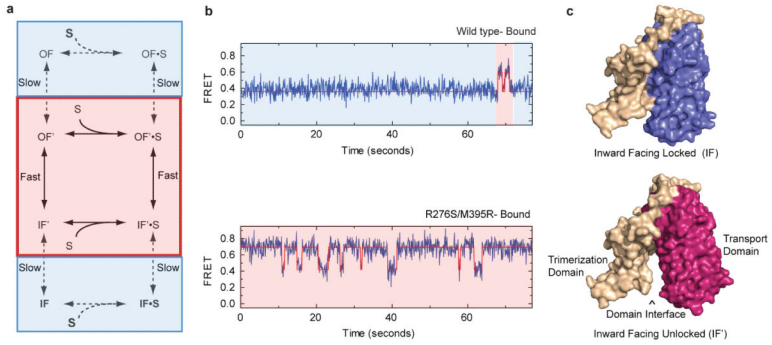

Figure 6. Kinetic model of transport

a, Schematic representation of the transport cycle. Red and blue boxes indicate dynamic and quiescent periods, respectively. **b,** Simulated single-molecule trajectories for WT Glt_{Ph} (top) and $H_{276,395}$-Glt_{Ph} (bottom). Periods of long-lived 'locked' states are shaded blue; periods of transitions between 'unlocked' states are shaded red. **c,** Structures of the inward-facing WT 'locked' state (top) and $H_{276,395}$-Glt_{Ph} 'unlocked' state (bottom).